A discontinuous Galerkin/cohesive zone model approach for the computational modeling of fracture in geometrically exact slender beams

Kota, Sai Kubair; Kumar, Siddhant; Giovanardi, Bianca

Important note
To cite this publication, please use the final published version (if applicable).
Please check the document version above.

ORIGINAL PAPER

A discontinuous Galerkin/cohesive zone model approach for the computational modeling of fracture in geometrically exact slender beams

Sai Kubair Kota[1,3] · **Siddhant Kumar**[2] · **Bianca Giovanardi**[1,3]

Abstract

Slender beams are often employed as constituents in engineering materials and structures. Prior experiments on lattices of slender beams have highlighted their complex failure response, where the interplay between buckling and fracture plays a critical role. In this paper, we introduce a novel computational approach for modeling fracture in slender beams subjected to large deformations. We adopt a state-of-the-art geometrically exact Kirchhoff beam formulation to describe the finite deformations of beams in three-dimensions. We develop a discontinuous Galerkin finite element discretization of the beam governing equations, incorporating discontinuities in the position and tangent degrees of freedom at the inter-element boundaries of the finite elements. Before fracture initiation, we enforce compatibility of nodal positions and tangents weakly, via the exchange of variationally-consistent forces and moments at the interfaces between adjacent elements. At the onset of fracture, these forces and moments transition to cohesive laws modeling interface failure. We conduct a series of numerical tests to verify our computational framework against a set of benchmarks and we demonstrate its ability to capture the tensile and bending fracture modes in beams exhibiting large deformations. Finally, we present the validation of our framework against fracture experiments of dry spaghetti rods subjected to sudden relaxation of curvature.

Keywords Slender beams · Geometrically exact beam formulation · Discontinuous Galerkin finite elements · Fracture mechanics · Cohesive zone models

1 Introduction

Slender beams are essential constituents of engineering materials and have a long history of serving as reinforcement elements in composite laminates [1], textiles [2], and paper products [3]. More recently, developments in additive manufacturing technology have enabled the combination of slender beams into engineered periodic truss lattices, giving rise to *truss architected materials* [4, 5]. In the wake of these technological advancements, there has been growing emphasis on designing optimal material microstructures capable of yielding specific target mechanical properties. For example, recent efforts within the scientific community have focused on designing material architectures aimed at achieving a desired anisotropic stiffness [6], optimal vibration control [7, 8], high specific stiffness and strength [9–11], and unprecedented specific impact energy absorption [12, 13]. While characterizing the failure modes of these materials is of paramount importance, particularly in the context of the performance-weight trade-off, the fracture mechanics of truss architected materials is not completely understood and remains an area of ongoing scientific interest.

Compression experiments on truss architected materials have highlighted the relevance of the interplay of buckling and fracture of the individual beam structural constituents in their overall failure response [9]. While buckling has been extensively studied in the literature in isolation, the interplay between buckling and fracture has traditionally received limited attention, perhaps due to the fact that buckling often leads to structural failure well before fracture initiation. More

✉ Bianca Giovanardi
b.giovanardi@tudelft.nl

1 Faculty of Aerospace Engineering, Delft University of Technology, 2629 HS Delft, The Netherlands

2 Department of Materials Science and Engineering, Delft University of Technology, 2628 CD Delft, The Netherlands

3 Delft Institute for Computational Science and Engineering, Delft University of Technology, 2628 CD Delft, The Netherlands

recently, as the structural engineering community has broadened its focus from developing buckling-safe structures to leveraging buckling instabilities as a design opportunity to create structures capable of adapting their shape to their surrounding environment [14–16], the study of the complex interplay between buckling and fracture in slender structures has gained increasing relevance.

Clearly, the complex fracture behavior of truss architected materials is significantly influenced by the combination of responses of the individual beam constituents. However, it is noteworthy that the buckling-to-fracture transition in a single slender beam already exhibits remarkable richness and complexity. A celebrated example is the fracture behavior of dry spaghetti rods, which consistently break into more than two pieces when subjected to large pure-bending stresses. This intriguing fracture behavior has puzzled numerous scientists, including the great physicist Richard Feynman [17]. Audoly and Neukirch later shed light on this phenomenon by uncovering a peculiar mechanical behavior of elastic rods in that the removal of stress leads to an *increase* in strain [18]. More specifically, the authors of that study theoretically predicted and confirmed through extensive experimentation that the sudden relaxation of curvature can trigger a burst of flexural waves, which locally increase the rod's curvature, ultimately leading to cascading fragmentation.

While physical experiments are essential for understanding the fracture mechanics of slender beams, computational approaches offer complementary insights, especially in scenarios where experimental methods become impractical or where the efficient exploration of extensive parameter spaces is necessary. Preliminary research efforts aimed at developing computational models for fracture in beams can be found in the works of Armero and Ehrlich [19], Becker and Noels [20] and, more recently, Lai et al. [21]. These studies are based on Euler–Bernoulli beam theory [22] but propose different approaches for fracture mechanics. Armero and Ehrlich [19] describe material failure via softening hinges modeled with the strong discontinuity approach. This approach, pioneered by Simo et al. [23], introduces discontinuities in the form of jumps of the solution field, which allow the characterization of the localized dissipative mechanisms associated with strain softening. Becker and Noels [20] adopt the discontinuous Galerkin / cohesive zone model approach, originally introduced by Radovitzky et al. [24]. This computational fracture mechanics approach employs a discontinuous Galerkin discretization of the governing equations and models fracture as a process of decohesion across interfaces between finite elements. In contrast, Lai et al. [21] describe the fracture process via a phase-field model [25, 26]. Although these computational models have been successful in modeling failure in beams exhibiting small deformations, they cannot be used to model buckling-to-fracture transition, due to the infinitesimal-deformations assumption inherent in the underlying Euler–Bernoulli beam theory [22]. Likewise, beam fracture models that rely on Timoshenko beam theory [22], e.g. [27–29], are also unsuitable for capturing the transition from buckling to fracture.

Clearly, a fundamental requirement for a computational model for fracture of beams experiencing significant deformations is its foundation in a beam model able to accurately describe geometric nonlinearities.[1] For example, Heisser et al. [31] found their beam fracture model on Kirchhoff beam theory, while Tojaga et al. [32] model fracture based on the finite-strain beam formulation by Simo [33]. More specifically, Heisser et al. [31] model the fragmentation of a beam by disconnecting adjacent elements instantaneously, upon satisfaction of a stress-based fracture criterion. However, this approach neglects the time-dependent aspects of the fracture process, which are known to be significant, particularly in the context of dynamic fragmentation [34, 35]. By contrast, Tojaga et al. [32] employ the strong discontinuity approach discussed above. In their work, the authors enrich the displacement field by introducing discontinuous modes at the elements midpoints. Beyond a critical load, they model failure at these discontinuities as a softening hinge. It is important to highlight that their approach models discontinuities exclusively in the displacement degrees of freedom, but not in the rotation degrees of freedom. As a consequence, their framework is capable of capturing fracture modes arising from tension and shear but not those resulting from bending.

In this paper, we present a computational framework to model the tensile and bending modes of fracture in slender beams subjected to finite deformation. We model the deformation of the beam with the geometrically exact torsion-free Kirchhoff beam finite element framework by Meier et al. [36, 37] and we adopt the discontinuous Galerkin/cohesive zone model (DG/CZM) approach for fracture mechanics. Specifically, we approximate the beam's deformation based on the finite element method using third-order Hermitian polynomial shape functions and mixed interpolation involving both position and tangent degrees of freedom. This choice is well-suited for the spatial discretization of the Kirchhoff beam formulation in view of the ability of third-order Hermitian polynomials to meet the C^1 continuity requirement. However, instead of imposing the compatibility strongly, we adopt a discontinuous Galerkin finite element approach and incorporate discontinuities in the position and tangent degrees of freedom at the inter-element boundaries of the finite elements. Before fracture initiation, we enforce compatibility of nodal positions and tangents weakly, via the exchange of variationally-consistent forces and moments at the interfaces between adjacent elements. At the onset of

---

[1] See the introduction of Meier et al. [30] for a recent review of geometrically exact beam models.
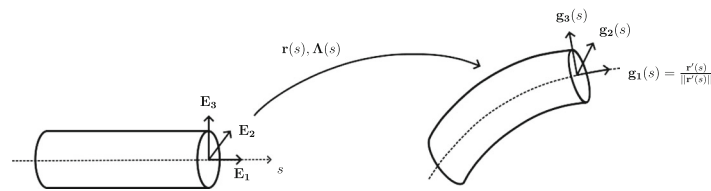
Fig. 1 Illustration of the kinematics of a geometrically exact Kirchhoff beam in the case of a beam with circular cross-section. The beam configuration is characterized by the line of centroids $r(s)$ and by the orthonormal *intrinsic* frame $\{g_1(s), g_2(s), g_3(s)\}$. The Kirchhoff constraint enforces that $g_1(s)$ be tangent to the line of centroids, that is $g_1(s) = \frac{r'(s)}{||r'(s)||}$

fracture, these variationally-consistent forces and moments transition to cohesive laws that model the fracture process. The finite element discretization described above results in a time-dependent algebraic system, which is solved in time with the second-order explicit Newmark scheme.

The resulting computational framework effectively captures both tensile and bending modes of fracture of slender beams in the geometrically nonlinear regime. Compared to existing state-of-the-art computational models for beam fracture, our approach offers the following key advantages. Unlike the model proposed by Heisser et al. [31], which lacks an energy dissipation mechanism, our approach is firmly rooted in a sound physical model for fracture mechanics. Consequently, it is able to describe the energy dissipation resulting from the fracture process, eliminating the need for ad-hoc measures such as enforcing a minimal fragment length to prevent unphysical crack formations [31]. Additionally, unlike the approach presented by Tojaga et al. [32], our approach is able to describe the bending fracture modes.

We conduct a series of numerical tests to verify our computational framework against a set of benchmarks and demonstrate its capability of accurately modeling tensile and bending fracture in slender beams exhibiting large deformations. First, we verify that the discontinuous Galerkin discretization is able to capture the analytical buckling load for a column. We then verify the discontinuous Galerkin/cohesive zone model fracture mechanics approach in a bar spall fracture benchmark. Next, we show that the incorporation of discontinuities in the tangent degrees of freedom is essential for capturing the bending mode of fracture. Finally, we apply our computational framework to reproduce experiments by Audoly and Neukirch [18] on the fracture of dry spaghetti rods bent and suddenly released.

The structure of the paper is as follows. In Sect. 2, we briefly review the geometrically exact Kirchhoff beam formulation of [33, 36]. Section 3 discusses the resultant based cohesive zone modeling approach for tensile and bending fracture of beams. In Sect. 4, we derive the discontinuous Galerkin weak formulation of the beam governing equations and the DG/CZM weak formulation to model the tensile and bending modes of fracture in slender beams. We, then, outline the space and time discretization of the DG/CZM weak form and discuss our solution strategy for the discrete system of equations. We perform thorough verification and validation of the computational framework in Sect. 6. Conclusions are drawn in Sect. 7.

2 Geometrically exact Kirchhoff beam formulation

For completeness, we provide a concise summary of the geometrically exact beam governing equations by Simo [33] in their shear-free variant, as derived by Meier et al. [36]. We refer the reader to those two works for a more detailed and comprehensive discussion.

2.1 Kinematics

Following Simo [33], we characterize the beam configuration by the position of the beam centerline and by the orientation of its cross-sections. The centerline of the beam, i.e. the curve of the cross-sections centroids, is described with a suitable parametrization $r(s) \in \mathbb{R}^3$, where $s \in [0, L]$ is the arc-length parameter, while the orientation of the beam cross-sections is described in terms of the orthonormal *intrinsic* frame $\{g_1(s), g_2(s), g_3(s)\}$, see Fig. 1. By convention, $g_1(s)$ is chosen orthogonal to the beam cross-section at s, while $g_2(s)$ and $g_3(s)$ are chosen parallel to its principal axes of inertia. Note that, in general, $g_1(s)$ is not tangent to the line of centroids $r(s)$.

The deformed configuration of the beam can be expressed in terms of r, g_2, and g_3 as:

$$x(s, \xi_2, \xi_3) = r(s) + \xi_2 \, g_2(s) + \xi_3 \, g_3(s), \qquad (1)$$

where ξ_2 and ξ_3 are coordinates on the beam cross-section in the reference configuration.

For simplicity, it is often assumed that the beam is straight in its reference configuration, so that the intrinsic frame in the reference configuration can be chosen as a fixed basis

$\{E_1, E_2, E_3\}$ of $\mathbb{R}^3$.[2] Because the vector basis $\{g_i(s)\}$ is orthonormal at any cross-section s, there exists a rotation tensor $\Lambda(s)$ such that:

$$g_i(s) = \Lambda(s)E_i, \quad i = 1, 2, 3. \tag{2}$$

Kinematically admissible variations of r and g_i are denoted with δr and δg_i, respectively. A direct consequence of Eq. (2) is that kinematically admissible variations of g_i can be expressed as

$$\delta g_i(s) = \delta\Lambda(s)\Lambda^T(s)g_i(s). \tag{3}$$

Because tensor $(\delta\Lambda)\Lambda^T$ is skew-symmetric, Equation (3) can be rewritten as

$$\delta g_i(s) = \delta\theta(s) \times g_i(s), \tag{4}$$

where $\delta\theta$ is the axial vector of $(\delta\Lambda)\Lambda^T$ and is also referred to as the *spin vector*. Under the hypothesis of negligible shear strains, which is a well-accepted assumption in the case of slender beams [36], $\delta\theta$ is not independent of $\delta r'$. In fact, a relation between $\delta\theta$ and $\delta r'$ can be obtained by kinematically enforcing that the beam centerline remain perpendicular to the cross-sections during the deformation (*Kirchhoff constraint*):

$$g_1(s) = \frac{r'(s)}{||r'(s)||}, \tag{5}$$

where $(\cdot)'$ denotes the derivative with respect to the arc-length parameter. Plugging Equation (5) into Eq. (4), we obtain the following relation:

$$\delta\theta(s) = \frac{r'(s) \times \delta r'(s)}{||r'(s)||^2} + \frac{r'(s)}{||r'(s)||}\delta\alpha,$$

prescribing the kinematically admissible variations of rotations $\delta\theta$ in terms of the kinematically admissible variations of the centerline tangents $\delta r'$ and the tangential component of the spin vector:

$$\delta\alpha(s) := \delta\theta(s) \cdot \frac{r'(s)}{||r'(s)||}.$$

where $\delta\alpha$ represents the kinematically admissible variation of the total twist angle. In this work, we limit our attention to the simpler torsion-free formulation and, following [37], we completely resign the degrees of freedom representing the torsional deformation modes, resulting in:

---

[2] This assumption is not fundamental and can be removed as discussed in [23].

$$\delta\theta(s) = \delta\theta_\perp(s) := \frac{r'(s) \times \delta r'(s)}{||r'(s)||^2}. \tag{6}$$

We refer the reader to [38] for a comprehensive discussion on the conditions under which a torsion-free beam formulation is appropriate.

2.2 Balance of linear and angular momentum

The governing equations of the beam can be derived by integrating the linear and angular momentum balance equations from the 3D continuum theory over the cross-section of the beam. We refer the reader to Simo [33] for a detailed derivation, while we report here only the final expressions:

$$f' + \tilde{f} = \rho A\ddot{r}, \tag{7}$$
$$m' + r' \times f + \tilde{m} = I_\rho\dot{\omega} + \omega \times (I_\rho\omega). \tag{8}$$

Here, the prime and dot symbols denote arc-length and material time derivatives, respectively, while ρ, A, and I_ρ are the referential mass density, area of cross-section, and spatial inertia tensor of the beam. ω is the axial vector corresponding to the the skew-symmetric angular velocity tensor $\dot{\Lambda}\Lambda^T$, while $f(s, t)$ and $m(s, t)$ are the internal force and moment stress resultants:

$$f = \int_A PE_1 \, dA, \tag{9}$$
$$m = \int_A (x - r) \times PE_1 \, dA, \tag{10}$$

where P is the Piola-Kirchhoff stress tensor. Finally, $\tilde{f}$ and $\tilde{m}$ are the external distributed forces and moments per unit referential arc-length.

Forces f, $\tilde{f}$ and moments m, $\tilde{m}$ can be additively decomposed into axial $f_{||}$, $\tilde{f}_{||}$ and shear $f_\perp$, $\tilde{f}_\perp$ forces, and bending $m_\perp$, $\tilde{m}_\perp$ and torsional $m_{||}$, $\tilde{m}_{||}$ moments, where the notation (11) is used.

$$a_{||} := \left(a \cdot \frac{r'}{||r'||}\right)\frac{r'}{||r'||}, \quad a_\perp := a - a_{||}. \tag{11}$$

Under the assumption that rotational inertia (i.e. the right-hand side of Eq. (8)) can be neglected, which is a well-accepted assumption for the case of slender beams [39, 40], the following equation expressing the internal shear forces as a function of the bending moments can be obtained by performing the cross product of Eq. (8) with r':

$$f_\perp = \frac{r'}{||r'||^2} \times \left(m_\perp' + \tilde{m}_\perp\right) \tag{12}$$

Equation (12) can be plugged into Equation (7), leading to:

$$f_{||}' + \left[\frac{r'}{||r'||^2} \times \left(m_\perp' + \tilde{m}_\perp \right) \right]' + \tilde{f} = \rho A \ddot{r}. \tag{13}$$

Note that, in the torsion-free formulation, Equation (12) is equivalent to Eq. (8). As a consequence, Eq. (13) is equivalent to the original system of governing equations (7) and (8). In this work, we focus on the simpler torsion-free case and we use Equation (13) to model the finite deformations of the beam.

Equation (13) is complemented with suitable initial conditions for positions and tangents, and boundary conditions, in terms of applied forces and bending moments on the Neumann boundary or imposed positions and tangents on the Dirichlet boundary.

2.3 Constitutive equations

In this study, we confine our attention to isotropic beams with circular cross-sections. Assuming hyperelastic material behavior, the internal axial forces and bending moments are related to the axial strain $\epsilon = ||r'|| - 1$ and the curvature $\kappa = \frac{r' \times r''}{||r'||^2}$ through the following constitutive relations [37]:

$$f_{||} = EA\epsilon \frac{r'}{||r'||}, \qquad m_\perp = EI\kappa, \tag{14}$$

where E, A and I are the Young's modulus, cross-sectional area and moment of inertia of the beam, respectively.
It should be emphasized that the constitutive relations (14) are only applicable in the context of small strains. Nevertheless, the proposed computational framework is general in the sense that the constitutive relations can be extended to incorporate various material behaviors. For instance, plasticity can be included to simulate fracture in metals, while viscoelasticity [41] or elasto-visco-plasticity [42] can be integrated to model fracture in 3D-printed polymers.

3 Cohesive zone approach for fracture in beams

We discuss the fracture modes of beams and propose cohesive laws to model the tensile and bending modes of beam fracture in this section. Beams exhibit several modes of fracture, which we illustrate in Fig. 2. In fact, beams can fail under tensile, transverse, torsional or bending loads. In this work, we focus our attention on the tensile and bending fracture modes in slender beams, while we neglect the shear and torsional fracture modes.

We adopt the cohesive zone approach to model the beam fracture behavior. Cohesive zone models employ a traction-
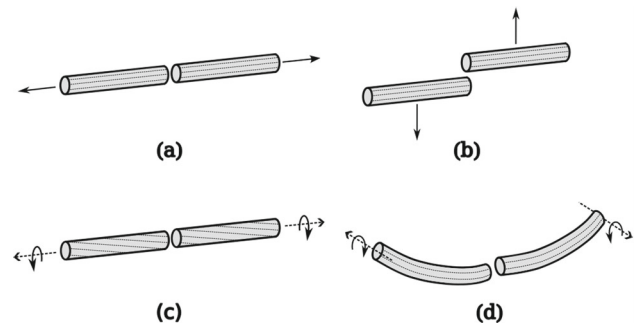

Fig. 2 The fracture modes of beams: **a** tension, **b** shear, **c** torsion and **d** bending

separation law to characterize the evolution of a crack, under the assumption that fracture processes occur within a region of finite-length ahead of the crack tip, referred to as the cohesive zone. However, instead of employing the conventional traction-separation laws typical in cohesive zone models [43], we formulate the cohesive laws in the stress resultant form, see [44, 45]. Following common practice in the cohesive zone modeling framework, we make the customary assumption that cohesive forces and moments depend solely on the kinematic jumps in the proximity of the crack tip.

We introduce cohesive boundaries at interfaces of adjacent elements of the beam, where jump discontinuities in the kinematic fields can occur. At these interfaces we define the axial and bending kinematic jumps $\Delta_{||}$ and Θ as:

$$\Delta_{||} = [\![r]\!] \cdot \hat{n}_{coh}$$
$$\Theta = [\![g_1]\!], \tag{15}$$

where $\hat{n}_{coh}$ is the unit normal to the cohesive boundary in the current configuration:

$$\hat{n}_{coh} = \frac{\langle g_1 \rangle}{||\langle g_1 \rangle||}. \tag{16}$$

and the notations

$$[\![\bullet]\!]\Big|_{s=a} := \lim_{s \to a^+} \bullet - \lim_{s \to a^-} \bullet$$
$$\langle \bullet \rangle \Big|_{s=a} := \frac{1}{2} \left(\lim_{s \to a^+} \bullet + \lim_{s \to a^-} \bullet \right)$$

represent the jump and average of the field $\bullet$ at any arbitrary point $s = a \in (0, L)$.
Note that Θ has a vanishing component along the normal to the cohesive boundary, as $\Theta \cdot \hat{n}_{coh} = 0$ holds by construction.

To enable mixed-mode fracture under tension and bending, we introduce a scalar effective separation Δ:

$$\Delta = \sqrt{\{\Delta_{||}\}^2 + \left(\alpha R ||\Theta|| \right)^2}, \tag{17}$$
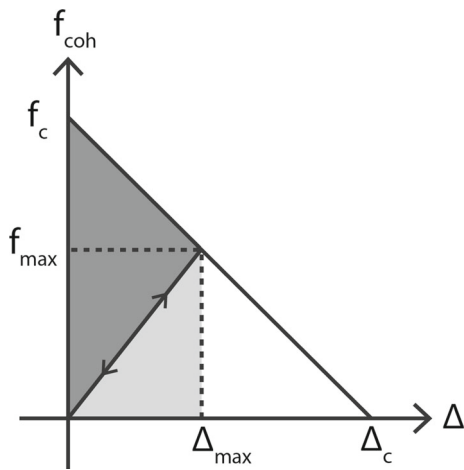
Fig. 3 The force-separation cohesive law prescribes a linear decay of the scalar effective cohesive force f_{coh} with the scalar effective separation Δ, from a critical value f_c to zero. Irreversibility is modeled by introducing a history variable Δ_{max} representing the maximum effective separation achieved. The unloading path follows a trajectory back to the origin, while reloading occurs on the same unloading path. The total area under the force-separation curve is equal to the effective fracture energy of the material while the black and grey areas at any point $\Delta = \Delta_{max}$ represent the dissipated and maximum recoverable energies at the cohesive boundary. Complete fracture is achieved when $\Delta \geq \Delta_c$

where R is the radius of the beam and α is a mode-mixity parameter, akin to that traditionally employed for mixed-mode cohesive laws [46]. In the equation above, $\{\cdot\} = \max(\cdot, 0)$ denotes the Macaulay operator.

We introduce the following cohesive axial forces and cohesive bending moments resisting the opening of cracks in the beam:

$$f_{coh, \parallel} = f_{coh}(\Delta, q) \frac{\{\Delta_{\parallel}\}}{\Delta} \hat{n}_{coh},$$

$$m_{coh, \perp} = \alpha^2 f_{coh}(\Delta, q) \frac{R^2}{\Delta} \Theta, \qquad (18)$$

where the effective cohesive force f_{coh} is a scalar function of the effective separation Δ and of a set of internal variables q. The function $f_{coh}(\Delta, q)$ can be tailored based on the desired representation of the constitutive fracture behavior (e.g. brittle, quasi-brittle, ductile). Here, we assume that cohesive axial forces and cohesive bending moments decay linearly with Δ, as illustrated in Fig. 3, and account for irreversibility by introducing a history internal variable Δ_{max}, as is customary in cohesive zone modeling.

Specifically, in the loading stage, we set:

$$f_{coh}(\Delta, \Delta_{max}) = \left(1 - \frac{\Delta}{\Delta_c}\right) f_c \quad \text{for} \quad \Delta \geq \Delta_{max}, \qquad (19)$$

where Δ_{max} is the maximum effective separation in the entire loading history, $\Delta_c = 2G_c/\sigma_c$ is the effective separation at

which complete decohesion occurs, and G_c is the effective fracture energy. In the unloading and reloading stage, we set:

$$f_{coh}(\Delta, \Delta_{max}) = \frac{\Delta}{\Delta_{max}} f_{max} \quad \text{for} \quad \Delta < \Delta_{max}, \qquad (20)$$

where f_{max} is the effective cohesive force at Δ_{max}.

The cohesive laws described above are activated at an inter-element boundary of the beam upon meeting the following fracture initiation criterion:

$$f_{eq}(\langle f \rangle, \langle m_{\perp} \rangle) \geq f_c, \qquad (21)$$

where $f_c = \sigma_c A$ is the critical effective cohesive force expressed in terms of the material's cohesive strength σ_c, and f_{eq} is an equivalent force given by the scalar:

$$f_{eq}(f, m_{\perp}) = \sqrt{\{f \cdot \hat{n}_{coh}\}^2 + \left\|\frac{m_{\perp}}{\alpha R}\right\|^2}. \qquad (22)$$

4 Computational framework for fracture in geometrically exact slender beams

In this section, we derive our discontinuous Galerkin/cohesive zone model approach for fracture in geometrically exact slender beams. We first derive the discontinuous Galerkin weak formulation of the beam governing equations presented in Sect. 2. We, then, present the weak formulation of the discontinuous Galerkin/cohesive zone model followed by its space and time discretization.

4.1 Derivation of the discontinuous Galerkin weak form

We consider a space discretization Ω_h of the straight undeformed beam Ω into segments $\Omega_e = (s_0^e, s_1^e)$, $e = 1, \ldots, E$, so that $\Omega_h = \bigcup_{e=1}^{E} \overline{\Omega}_e$, see schematic in Fig. 4. We denote with $\partial \Omega_h = \{0, L\}$ the boundary of the beam, whose external normal n_e is $n_e = 1$ at $s = L$ and $n_e = -1$ at $s = 0$. Finally, we denote with $\partial_{N_f} \Omega_h$ and $\partial_{N_m} \Omega_h$ the Neumann portions of $\partial \Omega_h$, where we apply forces $\bar{f}$ and moments $\bar{m}_{\perp}$, respectively.

We consider Eq. (13), where we allow $r(s)$ and its associated kinematically admissible variations $\delta r(s)$ to exhibit discontinuities at the interfaces s_n, $n = 1, \ldots, E - 1$ of adjacent elements. We start the derivation of the discontinuous Galerkin weak form of Eq. (13) by multiplying it with δr, integrating over the individual subdomains Ω_e,
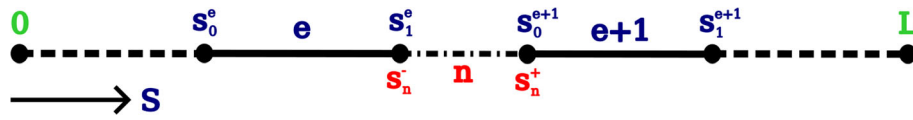
Fig. 4 The discontinuous Galerkin discretization of the straight undeformed beam. Internal nodes, e.g. nodes s_1^e and s_0^{e+1}, are duplicated to allow the embedding of potential discontinuities at the element interfaces s_n for $n = 1, \ldots, E-1$

$e = 1, \ldots, E$, and performing the integration by parts:

$$-\sum_{e=1}^{E} \int_{\Omega_e} \boldsymbol{f}_{\|} \cdot \delta \boldsymbol{r}' \, ds - \sum_{e=1}^{E} \int_{\Omega_e} \boldsymbol{f}_{\perp} \cdot \delta \boldsymbol{r}' \, ds$$

$$-\sum_{n=1}^{E-1} [\![\boldsymbol{f} \cdot \delta \boldsymbol{r}]\!] \Big|_{s_n} + \left(\bar{\boldsymbol{f}} \cdot \delta \boldsymbol{r} \right) \Big|_{\partial_{N_f} \Omega_h}$$

$$+\sum_{e=1}^{E} \int_{\Omega_e} \tilde{\boldsymbol{f}} \cdot \delta \boldsymbol{r} \, ds = \sum_{e=1}^{E} \int_{\Omega_e} \rho A \ddot{\boldsymbol{r}} \cdot \delta \boldsymbol{r} \, ds, \tag{23}$$

where we have applied the Neumann boundary condition $\bar{\boldsymbol{f}} = n_e \boldsymbol{f}$ on $\partial_{N_f} \Omega_h$. In Eq. (23), the notation $\bullet \big|_a$ means $\bullet$ evaluated at $s = a$.

Using the identity $[\![\boldsymbol{a} \cdot \boldsymbol{b}]\!] = \langle \boldsymbol{a} \rangle \cdot [\![\boldsymbol{b}]\!] + [\![\boldsymbol{a}]\!] \cdot \langle \boldsymbol{b} \rangle$, we can rewrite the jump term in Eq. (23) as:

$$\sum_{n=1}^{E-1} [\![\boldsymbol{f} \cdot \delta \boldsymbol{r}]\!] \Big|_{s_n} = \sum_{n=1}^{E-1} \left[\langle \boldsymbol{f} \rangle \cdot [\![\delta \boldsymbol{r}]\!] \right] \Big|_{s_n}$$

$$+ \sum_{n=1}^{E-1} \left[[\![\boldsymbol{f}]\!] \cdot \langle \delta \boldsymbol{r} \rangle \right] \Big|_{s_n}. \tag{24}$$

In addition, Eq. (12), together with the vector identity $\boldsymbol{a} \cdot (\boldsymbol{b} \times \boldsymbol{c}) = \boldsymbol{c} \cdot (\boldsymbol{a} \times \boldsymbol{b})$, allows us to rewrite the second term of Eq. (23) as:

$$-\sum_{e=1}^{E} \int_{\Omega_e} \boldsymbol{f}_{\perp} \cdot \delta \boldsymbol{r}' \, ds = \sum_{e=1}^{E} \int_{\Omega_e} (\boldsymbol{m}_{\perp}' + \tilde{\boldsymbol{m}}_{\perp}) \cdot \frac{\boldsymbol{r}' \times \delta \boldsymbol{r}'}{\|\boldsymbol{r}'\|^2} \, ds$$

$$= \sum_{e=1}^{E} \int_{\Omega_e} (\boldsymbol{m}_{\perp}' + \tilde{\boldsymbol{m}}_{\perp}) \cdot \delta \boldsymbol{\theta}_{\perp} \, ds. \tag{25}$$

Note that the kinematically admissible variation $\delta \boldsymbol{\theta}_{\perp}$ of Eq. (6) arises naturally as the work conjugate of the bending moments. In the following derivation, we will omit the subscript in $\delta \boldsymbol{\theta}_{\perp}$ and simply write $\delta \boldsymbol{\theta}$ for the sake of a lighter notation. The right-hand side of Eq. (25) can be, in turn, integrated by parts, leading to:

$$\sum_{e=1}^{E} \int_{\Omega_e} (\boldsymbol{m}_{\perp}' + \tilde{\boldsymbol{m}}_{\perp}) \cdot \delta \boldsymbol{\theta} \, ds = \sum_{e=1}^{E} \int_{\Omega_e} \tilde{\boldsymbol{m}}_{\perp} \cdot \delta \boldsymbol{\theta} \, ds$$

$$-\sum_{e=1}^{E} \int_{\Omega_e} \boldsymbol{m}_{\perp} \cdot \delta \boldsymbol{\theta}' \, ds - \sum_{n=1}^{E-1} \left[\langle \boldsymbol{m}_{\perp} \rangle \cdot [\![\delta \boldsymbol{\theta}]\!] \right] \Big|_{s_n}$$

$$-\sum_{n=1}^{E-1} \left[[\![\boldsymbol{m}_{\perp}]\!] \cdot \langle \delta \boldsymbol{\theta} \rangle \right] \Big|_{s_n} (\bar{\boldsymbol{m}}_{\perp} \cdot \delta \boldsymbol{\theta}) \Big|_{\partial_{N_m} \Omega_h}, \tag{26}$$

where we have applied the Neumann boundary condition $\bar{\boldsymbol{m}}_{\perp} = n_e \boldsymbol{m}_{\perp}$ on $\partial_{N_m} \Omega_h$ and used again the identity $[\![\boldsymbol{a} \cdot \boldsymbol{b}]\!] = \langle \boldsymbol{a} \rangle \cdot [\![\boldsymbol{b}]\!] + [\![\boldsymbol{a}]\!] \cdot \langle \boldsymbol{b} \rangle$.

Gathering Equations (23), (24), (25), and (26), we obtain:

$$\sum_{e=1}^{E} \int_{\Omega_e} \rho A \ddot{\boldsymbol{r}} \cdot \delta \boldsymbol{r} \, ds + \sum_{e=1}^{E} \int_{\Omega_e} \boldsymbol{f}_{\|} \cdot \delta \boldsymbol{r}' \, ds$$

$$+ \sum_{n=1}^{E-1} \left[\langle \boldsymbol{f} \rangle \cdot [\![\delta \boldsymbol{r}]\!] \right] \Big|_{s_n} + \sum_{n=1}^{E-1} \left[[\![\boldsymbol{f}]\!] \cdot \langle \delta \boldsymbol{r} \rangle \right] \Big|_{s_n}$$

$$+ \sum_{e=1}^{E} \int_{\Omega_e} \boldsymbol{m}_{\perp} \cdot \delta \boldsymbol{\theta}' \, ds + \sum_{n=1}^{E-1} \left[\langle \boldsymbol{m}_{\perp} \rangle \cdot [\![\delta \boldsymbol{\theta}]\!] \right] \Big|_{s_n}$$

$$+ \sum_{n=1}^{E-1} \left[[\![\boldsymbol{m}_{\perp}]\!] \cdot \langle \delta \boldsymbol{\theta} \rangle \right] \Big|_{s_n} = \sum_{e=1}^{E} \int_{\Omega_e} \tilde{\boldsymbol{f}} \cdot \delta \boldsymbol{r} \, ds$$

$$+ \left(\bar{\boldsymbol{f}} \cdot \delta \boldsymbol{r} \right) \Big|_{\partial_{N_f} \Omega_h} + \sum_{e=1}^{E} \int_{\Omega_e} \tilde{\boldsymbol{m}}_{\perp} \cdot \delta \boldsymbol{\theta} \, ds$$

$$+ (\bar{\boldsymbol{m}}_{\perp} \cdot \delta \boldsymbol{\theta}) \Big|_{\partial_{N_m} \Omega_h}, \tag{27}$$

Since jumps in forces $\boldsymbol{f}$ and bending moments $\boldsymbol{m}_{\perp}$ need not be penalized to ensure the consistency of the numerical scheme, the terms involving their jumps in Eq. (27) can be ignored, see also [20, 47]. However, the inter-element compatibility has to be enforced weakly to ensure the stability of the numerical scheme. Here, we do so through the interior penalty method, following [20, 47]. Specifically, we add the following terms to the left-hand side of Equation (27):

$$\sum_{n=1}^{E-1} \beta_p \left[\left\langle \frac{EA}{h} \right\rangle [\![\delta \boldsymbol{r}]\!] \cdot [\![\boldsymbol{r}]\!] \right] \Big|_{s_n}$$

$$+ \sum_{n=1}^{E-1} \beta_t \left[\left\langle \frac{EI}{h} \right\rangle [\![\delta \boldsymbol{g_1}]\!] \cdot [\![\boldsymbol{g_1}]\!] \right] \Big|_{s_n},$$

where we recall that $\boldsymbol{g_1} = \frac{\boldsymbol{r}'}{||\boldsymbol{r}'||}$ (see Eq. (5)), while $\beta_p > 1$ and $\beta_t > 1$ are position and tangent jump penalty parameters and h is the element size.

We, therefore, obtain the following stabilized discontinuous Galerkin weak form:

$$
\begin{aligned}
&\int_{\Omega_h} \rho A \ddot{\boldsymbol{r}} \cdot \delta \boldsymbol{r} \, ds \\
&+ \int_{\Omega_h} EA\, \varepsilon \, \delta\varepsilon \, ds + \sum_{n=1}^{E-1} \Big[\langle \boldsymbol{f} \rangle \cdot [\![\delta \boldsymbol{r}]\!] \Big] \Big|_{s_n} \\
&+ \sum_{n=1}^{E-1} \beta_p \Big[\Big\langle \frac{EA}{h} \Big\rangle [\![\boldsymbol{r}]\!] \cdot [\![\delta \boldsymbol{r}]\!] \Big] \Big|_{s_n} \\
&+ \int_{\Omega_h} EI\, \boldsymbol{\kappa} \cdot \delta\boldsymbol{\kappa} \, ds + \sum_{n=1}^{E-1} \Big[\langle \boldsymbol{m}_\perp \rangle \cdot [\![\delta\boldsymbol{\theta}]\!] \Big] \Big|_{s_n} \\
&+ \sum_{n=1}^{E-1} \beta_t \Big[\Big\langle \frac{EI}{h} \Big\rangle [\![\boldsymbol{g_1}]\!] \cdot [\![\delta\boldsymbol{g_1}]\!] \Big] \Big|_{s_n} \\
&= \int_{\Omega_h} \tilde{\boldsymbol{f}} \cdot \delta \boldsymbol{r} \, ds + \Big(\bar{\boldsymbol{f}} \cdot \delta \boldsymbol{r} \Big) \Big|_{\partial_{N_f}\Omega_h} + \int_{\Omega_h} \tilde{\boldsymbol{m}}_\perp \cdot \delta\boldsymbol{\theta} \, ds \\
&+ (\bar{\boldsymbol{m}}_\perp \cdot \delta\boldsymbol{\theta}) \Big|_{\partial_{N_m}\Omega_h},
\end{aligned}
\tag{28}
$$

where we have also applied the constitutive relations (14).

4.2 The discontinuous Galerkin/cohesive zone model (DG/CZM) weak formulation

As discussed in Sect. 4.1, within the discontinuous Galerkin formulation, the position and tangent fields are allowed to exhibit discontinuities at the boundaries of the finite elements. However, prior to fracture, the solution's compatibility across element boundaries is maintained via the variationally-consistent interface forces and moments derived in that section.

Upon satisfaction of the fracture criterion (21), the interface axial forces and bending moments in Equation (28) are replaced with the cohesive axial forces and the cohesive bending moments of Equation (18). However, because we assume negligible shear strains and, consistently, we do not model the shear modes of fracture, we ensure that the component of the interface force term perpendicular to the unit normal of the cohesive boundary in Eq. (28) remains active until complete interface failure [20]. Specifically, this is achieved by introducing two binary parameters α_n and γ_n, which take value at each interface n. While we set both $\alpha_n = 1$ and $\gamma_n = 1$ before fracture initiation, we set $\alpha_n = 0$ after the fracture criterion (21) is met, and $\gamma_n = 0$ upon complete decohesion (i.e. $\Delta \geq \Delta_c$).

The discontinuous Galerkin/cohesive zone model weak form reads, therefore:

$$
\begin{aligned}
&\int_{\Omega_h} \rho A \ddot{\boldsymbol{r}} \cdot \delta \boldsymbol{r} \, ds \\
&+ \int_{\Omega_h} EA\, \varepsilon \, \delta\varepsilon \, ds + \sum_{n=1}^{E-1} \alpha_n \Big[\boldsymbol{f}_{DG,\,\|} \cdot [\![\delta \boldsymbol{r}]\!] \Big] \Big|_{s_n} \\
&+ \sum_{n=1}^{E-1} \gamma_n \Big[\boldsymbol{f}_{DG,\,\perp} \cdot [\![\delta \boldsymbol{r}]\!] \Big] \Big|_{s_n} \\
&+ \sum_{n=1}^{E-1} \alpha_n \Big[\beta_p \Big\langle \frac{EA}{h} \Big\rangle \boldsymbol{c}_{DG,\,\|} \cdot [\![\delta \boldsymbol{r}]\!] \Big] \Big|_{s_n} \\
&+ \sum_{n=1}^{E-1} \gamma_n \Big[\beta_p \Big\langle \frac{EA}{h} \Big\rangle \boldsymbol{c}_{DG,\,\perp} \cdot [\![\delta \boldsymbol{r}]\!] \Big] \Big|_{s_n} \\
&+ \int_{\Omega_h} EI\, \boldsymbol{\kappa} \cdot \delta\boldsymbol{\kappa} \, ds + \sum_{n=1}^{E-1} \alpha_n \Big[\langle \boldsymbol{m}_\perp \rangle \cdot [\![\delta\boldsymbol{\theta}]\!] \Big] \Big|_{s_n} \\
&+ \sum_{n=1}^{E-1} \alpha_n \Big[\beta_t \Big\langle \frac{EI}{h} \Big\rangle [\![\boldsymbol{g_1}]\!] \cdot [\![\delta\boldsymbol{g_1}]\!] \Big] \Big|_{s_n} \\
&+ \sum_{n=1}^{E-1} (1 - \alpha_n) \Big[\boldsymbol{f}_{coh,\,\|} \cdot [\![\delta \boldsymbol{r}]\!] \Big] \Big|_{s_n} \\
&+ \sum_{n=1}^{E-1} (1 - \alpha_n) \Big[\boldsymbol{m}_{coh,\,\perp} \cdot [\![\delta\boldsymbol{g_1}]\!] \Big] \Big|_{s_n} \\
&= \int_{\Omega_h} \tilde{\boldsymbol{f}} \cdot \delta \boldsymbol{r} \, ds + \Big(\bar{\boldsymbol{f}} \cdot \delta \boldsymbol{r} \Big) \Big|_{\partial_{N_f}\Omega_h} + \int_{\Omega_h} \tilde{\boldsymbol{m}}_\perp \cdot \delta\boldsymbol{\theta} \, ds \\
&+ (\bar{\boldsymbol{m}}_\perp \cdot \delta\boldsymbol{\theta}) \Big|_{\partial_{N_m}\Omega_h}
\end{aligned}
\tag{29}
$$

where we have set:

$$
\begin{aligned}
\boldsymbol{f}_{DG,\,\|} &= \big(\langle \boldsymbol{f} \rangle \cdot \hat{\boldsymbol{n}}_{coh} \big) \, \hat{\boldsymbol{n}}_{coh}, \\
\boldsymbol{f}_{DG,\,\perp} &= \big(\boldsymbol{I} - \hat{\boldsymbol{n}}_{coh} \otimes \hat{\boldsymbol{n}}_{coh} \big) \langle \boldsymbol{f} \rangle, \\
\boldsymbol{c}_{DG,\,\|} &= \big([\![\boldsymbol{r}]\!] \cdot \hat{\boldsymbol{n}}_{coh} \big) \, \hat{\boldsymbol{n}}_{coh}, \\
\boldsymbol{c}_{DG,\,\perp} &= \big(\boldsymbol{I} - \hat{\boldsymbol{n}}_{coh} \otimes \hat{\boldsymbol{n}}_{coh} \big) [\![\boldsymbol{r}]\!].
\end{aligned}
$$

Finally, in the event of recontact of the cracked surfaces after fracture initiation (i.e. when $\Delta_\| < 0$ and $\Delta_{max} > 0$), we reactivate the variationally-consistent axial forces and the position stabilization term, so as to allow propagation of compressive stress waves across cracked interfaces.

4.3 Discretization in space and time

We discretize $\boldsymbol{r}$ in space with third-order Hermite polynomials, which are shown to yield convergence order of four in continuous Galerkin settings, see [30]. The preference for Hermite polynomials over Lagrange polynomials stems from

the advantage that the arc-length derivative r' at each node is directly available as a primary degree of freedom associated with that particular node, which simplifies the computation of the terms at the element interfaces in Eq. (28). We therefore discretize r as follows:

$$r(\xi) \approx \sum_{b=1}^{2} N_p^b(\xi)\, p^b + \frac{L}{2} \sum_{b=1}^{2} N_t^b(\xi)\, t^b := \sum_{a=1}^{4} N_a(\xi)\, x_a,$$

(30)

where p^b and t^b are the position and tangent degrees of freedom at the element nodes $b = 1, 2$, $\xi \in [-1, 1]$ is the parametric coordinate in the reference element, which is mapped to the arc-length coordinate $s \in [0, L]$ as $s = \frac{L}{2}(1 + \xi)$, and N_p^b and N_t^b are the following shape functions:

$$N_p^1(\xi) = \frac{1}{4}(2 + \xi)(1 - \xi)^2 ; \quad N_p^2(\xi) = \frac{1}{4}(2 - \xi)(1 + \xi)^2,$$

$$N_t^1(\xi) = \frac{1}{4}(1 + \xi)(1 - \xi)^2 ; \quad N_t^2(\xi) = -\frac{1}{4}(1 - \xi)(1 + \xi)^2.$$

This space discretization results in the following semi-discrete system of equations:

$$M_{ab}\ddot{x}_b + f_a^{int} + f_{a\pm}^{jump} = f_a^{ext},$$

(31)

where the inertia $M_{ab}\ddot{x}_b$, internal (bulk) f_a^{int}, internal (interface) $f_{a\pm}^{jump}$, and external f_a^{ext} forces are reported in "Appendix A".

Given the strong nonlinearities involved with fracture, we opted for an explicit time discretization for simplicity. Specifically, we discretize Eq. (31) in time using the second-order explicit Newmark scheme. We perform a special mass lumping [48] to avoid the cost of solving a linear system for computing the accelerations. As explicit time stepping schemes are conditionally stable, we compute the stable time step Δt_c from the Courant-Friedrichs-Lewy condition:

$$\Delta t_c = \frac{2}{\omega_{max}},$$

(32)

where $\omega_{max} = \max_{i=1}^{N}(||\lambda_i||)$ is the maximum natural frequency of the system.

In our simulations, we compute the stable time step Δt_c only once at the beginning of the calculation and we set $\Delta t = \Delta t_c$ for the entire calculation. Specifically, we calculate Δt_c by solving the following linearized eigenvalue problem:

$$\left(K_{ab}^{int} + K_{ab\pm}^{jump, DG} - \lambda^2 M_{ab}^{lump} \right) \Phi = 0,$$

(33)

where λ and Φ are the eigenvalue and eigenvector pair, M_{ab}^{lump} is the lumped mass matrix, and the stiffness matrices

Table 1 Physical properties used in the bending of a cantilever beam benchmark

Property	Value
Length (L)	1 m
Radius (R)	0.01 m
Young's modulus (E)	200.0 GPa

K_{ab}^{int} and $K_{ab\pm}^{jump, DG}$ are reported in "Appendix B". It should be noted that the eigenvalues obtained by solving Eq. (33) may be complex since matrix $K_{ab\pm}^{jump, DG}$ is not symmetric.

5 Convergence analysis of the discontinuous Galerkin discretization

This section presents a convergence analysis of the discontinuous Galerkin space discretization in the geometrically nonlinear regime.
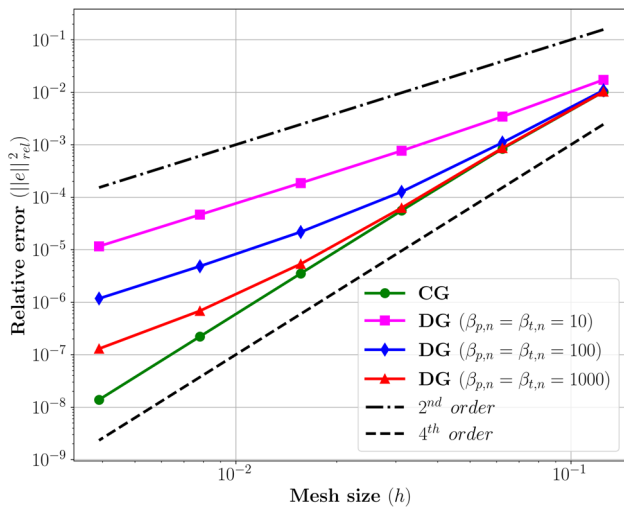
5.1 Bending of a cantilever beam

In this example, we analyze the convergence of the discontinuous Galerkin finite element discretization on a benchmark from Simo and Vu-Quoc [49]. We consider a cantilever beam of length L, radius R and Young's modulus E with a concentrated end moment of magnitude $M = \pi^2 E R^4 / L$, causing the beam to wind around itself twice forming a double circle. Table 1 summarizes the physical properties used in this problem.

We consider uniform meshes with element sizes starting at 0.125 m up to six levels of refinement, where each mesh refinement reduces the element size by a factor of 2. We also vary the penalty parameters ($\beta_{p,n}$ and $\beta_{t,n}$) amongst three values, namely 10, 100 and 1000, to investigate their influence on the convergence order of the framework. We solve this problem with our discontinuous Galerkin discretization in a quasi-static setting using a Newton–Raphson solver (linearization provided in "Appendix B") by applying the concentrated end moment in 50 load steps for each case. Following [36], we calculate the error in the deformed position of the beam centerline with the following relative L^2 norm:

$$||e||_{rel}^2 = \frac{1}{u_{max}} \sqrt{\frac{1}{L} \int_0^L ||r_h - r_{ref}||^2 \, ds}$$

(34)

where r_h and r_{ref} are the numerical and reference (analytical) beam centerline positions respectively and u_{max} is the maximum displacement obtained in a particular case.

The results of the convergence analysis are shown in Fig. 5. We observe that the convergence order of the discontinu-

Fig. 5 Convergence analysis of the discontinuous Galerkin (DG) finite element discretization for the bending of a cantilever beam benchmark. The plot shows the relative L^2 error in the deformed beam centerline positions as a function of the mesh size for different penalty parameter values ($\beta_{p,n}$ and $\beta_{t,n}$). Reference lines representing the convergence orders two and four are shown with dotted lines. The convergence order of the DG discretization approaches four, which is the expected value for a continuous Galerkin (CG) discretization, for higher values of the penalty parameters. Convergence deteriorates for smaller values of the penalty parameters

ous Galerkin finite element discretization approaches the expected value of four, as obtained in the continuous Galerkin setting [36], for increasing values of the penalty parameters, while it deteriorates for smaller values of $\beta_{p,n}$ and $\beta_{t,n}$. Our results are consistent with the findings by Brezzi et al. [50] that suggest the need for large penalty parameters to achieve the expected order of convergence in penalty based DG methods, especially for higher order polynomials. However, in implicit analyses, large penalty parameters lead to a large condition number of the stiffness matrix [50], resulting in an increased number of iterations for convergence of iterative linear solvers and in a larger simulation runtime. Conversely, in explicit analyses, large penalty parameters result in smaller stable time steps [51], thus also increasing the simulation runtime. Therefore, $\beta_{p,n}$ and $\beta_{t,n}$ should be chosen considering the usual tradeoff between accuracy and computational time. Nevertheless, a relative error of less than 1% and a consistent reduction in the error with h-refinement is observed across all examined mesh sizes and penalty parameter values.

6 Results

This section presents verification and validation of our computational framework.

Fig. 6 Schematic of the geometry and boundary conditions for the slender column buckling benchmark. The column is supported with a pin at the bottom end, a roller at the top end, and is loaded with an imposed axial displacement Δ. To facilitate the occurrence of the buckling bifurcation, a small, transverse perturbation force P is applied at the center of the column to break the problem's symmetry
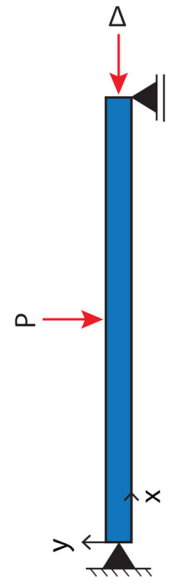
6.1 Framework verification: buckling of a slender column

We first verify our computational framework in the absence of fracture for the case of a column buckling under quasi-static axial compression. Specifically, we consider a slender column of length L, radius R and Young's modulus E and we verify that the first buckling mode occurs at Euler's critical axial force:

$$f_{cr} = \frac{\pi^3}{4} \frac{E R^4}{L^2}. \tag{35}$$

The problem geometry and boundary conditions considered are illustrated in Fig. 6. We apply a pin support at the bottom end of the column ($x = y = 0$), and a roller support allowing displacement in the x-direction at the top end ($x = L$, $y = 0$), where we also impose a displacement in the negative x direction, ramping up quasi-statically to a maximum Δ through 1000 load steps. In addition, we apply a constant perturbation force P at the center of the column ($x = L/2$, $y = 0$) as a means to break the symmetry of the problem. Table 2 summarizes the physical properties and numerical parameters used.

We apply our DG/CZM computational framework to solve the problem in a quasi-static setting using a Newton–Raphson solver with the linearization provided in "Appendix B". Figure 7 shows that the load–displacement response of the column is in agreement with the theoretical predictions.

6.2 Framework verification: fracture of a slender bar under tension

We verify the fracture modeling capability of our computational framework by simulating the spall of a bar, i.e. the development of a crack as a result of the interaction of two

Table 2 Physical properties and numerical parameters used in the slender column buckling benchmark

Property/parameter	Value
Length (L)	10 m
Radius (R)	0.1 m
Young's modulus (E)	200.0 GPa
Final applied displacement (Δ)	5.0 mm
Applied perturbation force (P)	1.0 N
Mesh size (h)	1.0 m
Penalty parameters ($\beta_{p,n}$ and $\beta_{t,n}$)	10
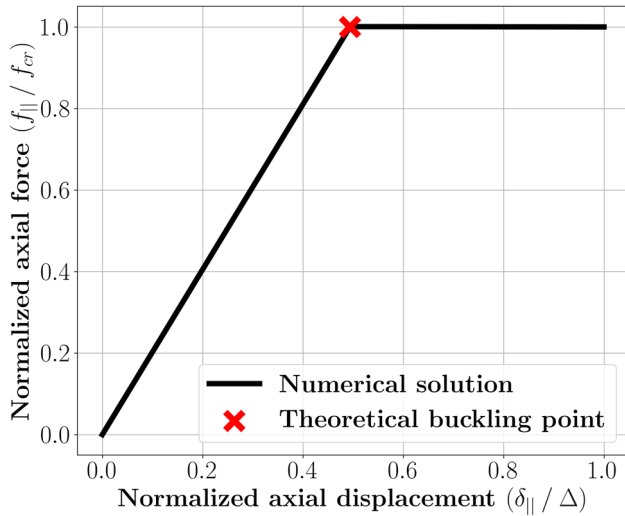
Fig. 7 Verification of our computational framework in the case of buckling of a slender column. The plot shows the force-displacement response at the top end of the column. The axial force $f_{\|}$ is normalized with respect to the theoretical critical axial force f_{cr}, while the axial displacement $\delta_{\|}$ is normalized with respect to the final applied displacement Δ. The theoretical buckling point is marked with a cross

tensile stress waves. We consider a slender bar subjected to tensile axial loading, while transverse displacement is restrained through roller supports at the bar ends, as illustrated in Fig. 8. We apply the following axial displacement signal:

$$\delta(t) = \frac{\sigma_f}{2} \frac{t}{\rho c_l}, \tag{36}$$

where $c_l = \sqrt{E/\rho}$ is the bar longitudinal wave speed and σ_f is a stress loading factor. Table 3 summarizes the physical properties and the numerical parameters used in this computational experiment.

We apply our DG/CZM computational framework to model the dynamic response of the bar with two values of σ_f, namely $\sigma_f = 0.1 \sigma_c$ and $\sigma_f = \sigma_c$. Figure 9 presents the evolution of the axial stress response over time obtained in our simulations, against the corresponding analytical solution to

Fig. 8 Schematic of the geometry and boundary conditions for the bar spall benchmark. The axial displacement signal $\delta(t)$ in Equation (36) is applied at the two ends of the bar, while two roller supports restrain the transverse displacement

Table 3 Physical properties and numerical parameters used in the bar spall benchmark

Property/parameter	Value
Length (L)	0.1 m
Radius (R)	1.0 mm
Mass density (ρ)	3690 kg m^{-3}
Young's modulus (E)	260.0 GPa
Critical cohesive strength (σ_c)	400.0 MPa
Fracture energy (G_c)	100.0 N m^{-1}
Mode-mixity parameter (α)	1
Simulation time (T)	10 µs
Mesh size (h)	0.1 mm
Time step (Δt)	0.01 ns
Penalty parameters ($\beta_{p,n}$ and $\beta_{t,n}$)	10
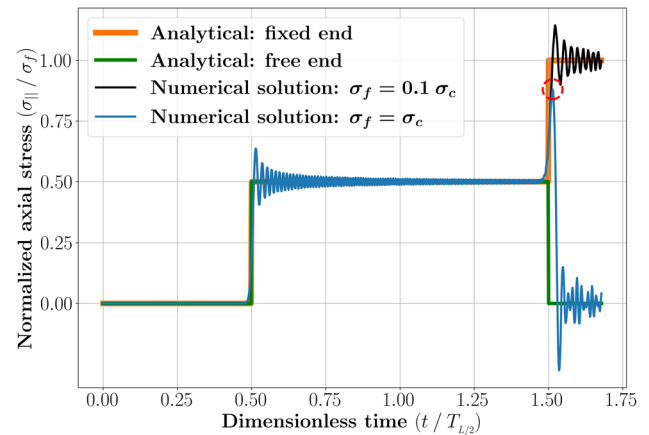
Fig. 9 Verification of our computational framework applied to the fracture of a slender bar under tensile load. The plot shows a comparison of the simulated and theoretical axial stress evolution in time, gauged at a point $L/4$ from the bar end, for two different applied displacement signals (Eq. (36)), one with $\sigma_f < \sigma_c$ (no fracture) and the other with $\sigma_f = \sigma_c$ (fracture). The theoretical predictions correspond to the solution of the 1D wave equation on a bar of half length with the same applied displacement signal on one end and the other end fixed (no fracture) or free (fracture). The axial stress $\sigma_{\|} = E\varepsilon$ is normalized with respect to the applied stress σ_f, while the time is normalized with respect to $T_{L/2} = L/(2c_l)$, which is the time when the longitudinal stress waves meet at the center of the bar. When $\sigma_f < \sigma_c$, our numerical results closely match the theoretical response of an uncracked bar. Conversely, at $\sigma_f = \sigma_c$, our results accurately capture the fracture event at $t = T_{L/2}$ due to the interaction of two tensile waves, the development of the release wave (see red circle) followed by the vanishing of the axial force due to fully developed fracture at the center of the beam

Fig. 10 Snapshots of pre-fracture and post-fracture evolution of the bar deformation and axial force at times: **a** 0.42 $T_{L/2}$, **b** 0.84 $T_{L/2}$, (c) 1.26 $T_{L/2}$, and (d) 1.68 $T_{L/2}$. The bar is shown in its deformed configuration (displacements are scaled by a factor of 10 for better visualization) and the contours show the axial forces in the bar. We observe the propagation of the two tensile step waves towards the center of the bar (**a** and **b**), the creation of a fracture surface as a result of their interaction at the center, as well as the reflection of the stress waves at the newly created free surface (**c** and **d**)
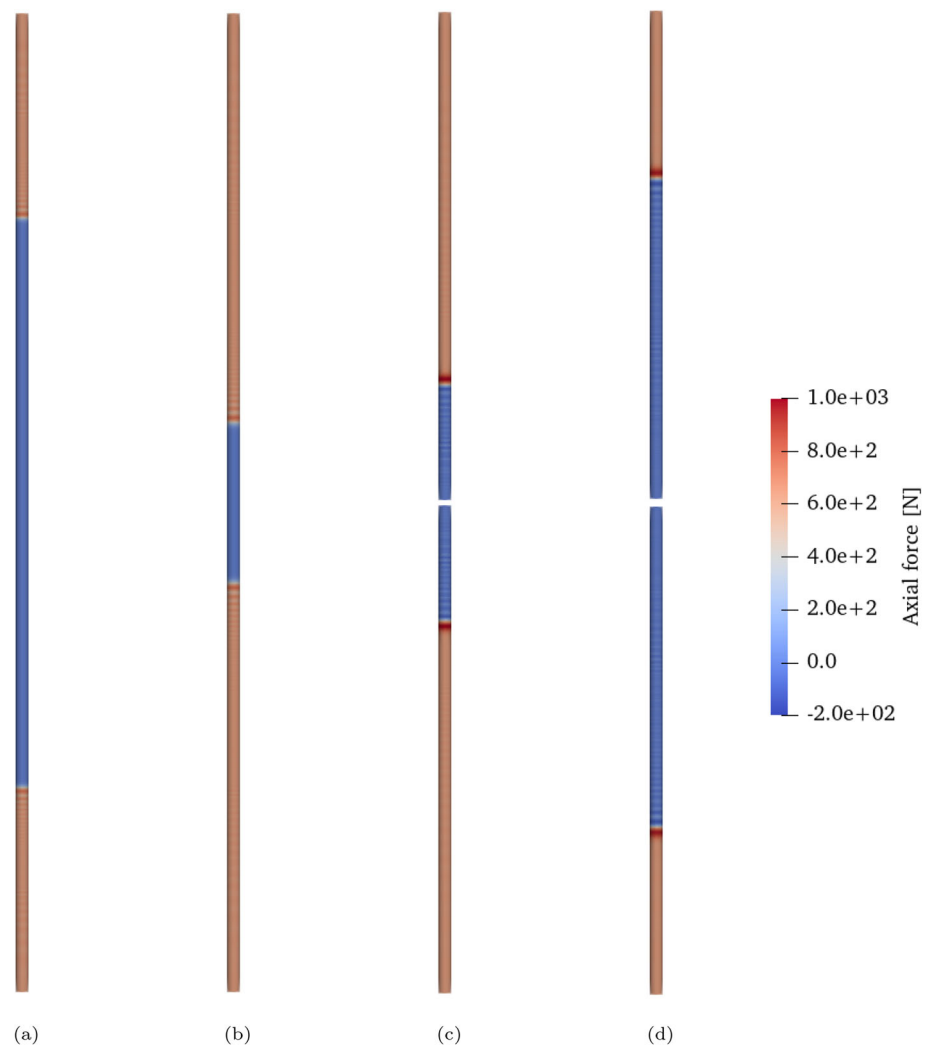
the 1D wave equation. It can be observed that the applied displacement signal generates two tensile stress waves with step waveform and intensity $\sigma_f/2$ propagating inwards from the beam ends. The two tensile waves meet at the center of the bar, building up a tensile stress wave of intensity σ_f. When σ_f is less than the critical fracture strength σ_c, our results show that the bar remains undamaged, as expected. When σ_f is equal to the critical fracture strength σ_c, our results capture the fracture response, including the development of a release wave and the subsequent vanishing of the axial stress due to the creation of a free surface. Figure 10 presents snapshots of the simulated bar response showing the bar deformation the propagation of the stress waves in the bar before and after fracture.

6.3 Fracture of a bar under transverse load

Through this example, we demonstrate the significance of incorporating inter-element jumps in the tangent (rotational) degrees of freedom and of modeling the relaxation of the bending moments as a function of these jumps, in the spirit of the well-established traction-separation laws of fracture mechanics. This is in contrast to the computational framework for fracture in geometrically exact beams proposed by Tojaga et al. [32], where only the displacement degrees of freedom are enriched with discontinuous modes, but not the rotational ones.

We consider a slender bar cantilevered at both ends and loaded at the center, as illustrated in Fig. 11. Specifically, we apply a time-dependent transverse displacement $\delta(t)$:

$$\delta(t) = \tilde{v}t \tag{37}$$

where $\tilde{v}$ is a sufficiently low loading rate to achieve quasi-static conditions. Table 4 summarizes the physical properties and the numerical parameters used in this computational experiment.

We solve this problem computationally with two different approaches: (1) our DG/CZM computational framework as described in Sect. 4, and (2) a variant of such frame-
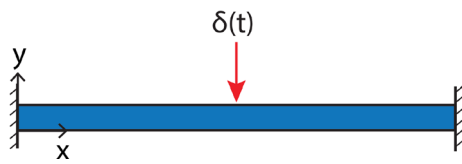
Fig. 11 Schematic of the geometry and boundary conditions for the problem of a bar under transverse load. The beam is cantilevered at both ends and loaded at the center with a time-dependent transverse displacement $\delta(t)$, see Eq. (37)
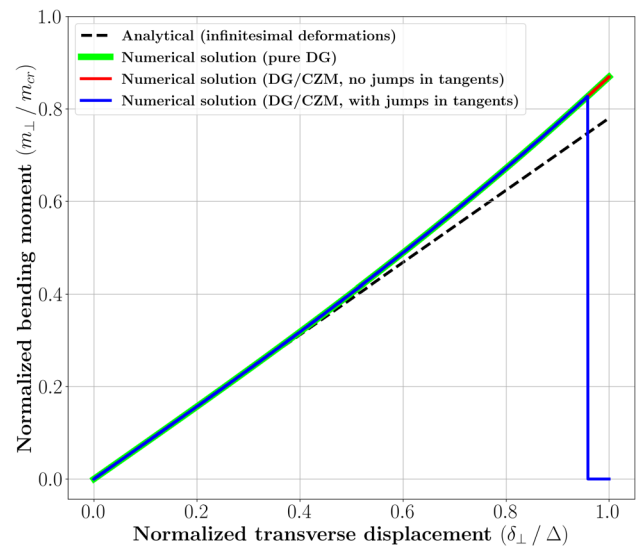
Table 4 Physical properties and numerical parameters used in the bar under transverse load problem

Property/parameter	Value
Length (L)	0.1 m
Radius (R)	1.0 mm
Mass density (ρ)	3690 kg m^{-3}
Young's modulus (E)	260.0 GPa
Critical cohesive strength (σ_c)	400.0 MPa
Fracture energy (G_c)	100.0 N m^{-1}
Mode-mixity parameter (α)	1
Load rate ($\tilde{v}$)	0.01 m s^{-1}
Simulation time (T)	0.2 s
Mesh size (h)	0.1 mm
Time step (Δt)	0.1 μs
Penalty parameters ($\beta_{p,n}$ and $\beta_{t,n}$)	10

Fig. 12 The load–displacement response at the center of a bar fracturing under transverse load, in terms of bending moment versus applied transverse displacement. Simulation results are plotted on top of the analytical predictions of Euler–Bernoulli beam theory (dashed line) to highlight the departure from the geometrically linear regime. The bending moment is normalized with respect to the critical bending moment $m_{cr} = AR\sigma_c$, where A is the area of the beam cross section, while the transverse displacement of the beam is normalized with respect to the maximum applied transverse displacement $\Delta = \tilde{v}T$. The plot compares simulation results from our DG/CZM framework with (blue line) and without (red line) discontinuities in tangent degrees of freedom. In the former case, bar failure under bending is accurately captured, resulting in a drop in bending moment, while in the latter case, fracture behavior is absent, and the bending moment follows a response predicted by a simulation without an embedded fracture mechanics model (green line). (Color figure online)

work that does not model the bending moment decay with the increasing tangents jumps (i.e. removing the bending moment term in Eq. (22)). Figure 12 compares the load–displacement responses of the center of the bar obtained with these two approaches. The figure shows the bending moments build-up with the increasing applied displacement, including the transition from the geometrically linear to the geometrically nonlinear regime. We observe that our DG/CZM approach is able to capture the fracture behavior arising from a further increase in applied displacement, along with the vanishing bending moment in the post-fracture behavior. This stands in stark contrast to the second approach, which predicts a load–displacement response identical to that of a simulation without an embedded fracture mechanics model (pure DG). This demonstrates the essential role of explicitly modeling jumps in the tangent degrees of freedom to capture the bending fracture mode.

We also observe that, under these conditions, fracture occurs in mixed bending and tensile modes, as complete fracture is achieved for an internal moment $m_\perp \approx 0.8 \, m_{cr} < m_{cr}$, where $m_{cr} = AR\sigma_c$, where A is the area of the beam cross section, see Fig. 12.

Figure 13 presents snapshots of the simulated bar response showing the bar configuration before and after fracture.

Note that in this physical scenario, the occurrence of fracture within the beam is anticipated both at its supports and at the center. However, our computational framework does not describe fracture at the supports as it limits the possible fracture initiation sites to the inter-element boundaries. While our computational framework can be adapted to model fracture at the beam's ends as well, we did not pursue that route, as the purpose of this example was purely to illustrate the significance of incorporating inter-element jumps in tangent (rotational) degrees of freedom when modeling the bending mode of fracture.

6.4 Framework validation: fracture of a bar bent and suddenly released

In this section, we validate our computational framework against experiments by Audoly and Neukirch [18] on the fragmentation of dry spaghetti. Specifically, that work presents experiments on dry spaghetti rods initially bent into an arc of circle and suddenly released at one end, while the other end remains clamped. The experiments show that this

Fig. 13 Snapshots of the simulated bar response before (top picture, $\delta(t) = 1.0\ mm$) and after (bottom picture, $\delta(t) = 1.92\ mm$) fracture. The bar is shown in its deformed configuration (displacements are scaled by a factor of 2 for better visualization) and the contours show the transverse displacement
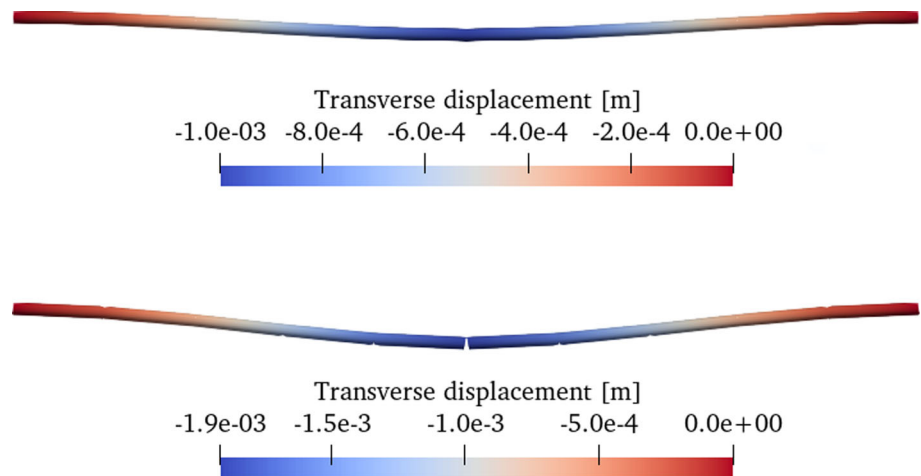
sudden relaxation of curvature results in a burst of flexural waves, which locally increase the curvature of the rod, ultimately leading to fracture.

We model these experiments with a two-stage solution strategy. As in experiments [18], the spaghetti rod remains clamped at one end in both stages of the analysis. In the first stage, we perform a quasi-static simulation using a Newton–Raphson solver with the linearization provided in "Appendix B" to bring the spaghetti rod to a curvature κ_0. Specifically, we apply a nodal moment of $EI\kappa_0$ at the free end of the rod in 10 load steps. Note that this initial pre-loading stage is necessary because of our model's assumption that the beam be straight in the reference (unstressed) configuration. The state achieved through the quasi-static pre-loading stage is then used as the initial condition for a dynamic simulation starting with the release of the spaghetti rod's free end. The physical properties and numerical parameters used in this computational experiment are summarized in Table 5. Specifically, we used the length L, radius R, and density ρ values reported in Heisser et al. [31] and we computed the Young's modulus E of the spaghetti rods with the formula $E = \gamma^2 \rho A/I$, where $\gamma = 0.521\ \mathrm{m}^2/\mathrm{s}$, see [18]. Finally, we obtained σ_c, and G_c based on the time and deformation shape of the rod reported in the experiments just before fracture.

Figure 14 shows contours of bending moments on the deformed spaghetti rods, superimposed to the experimentally observed deformed shapes at different times. Our DG/CZM framework accurately captures the fracture mechanism observed in the experiments, including the burst of flexural waves and the curvature build-up in the proximity of the clamped end.

7 Conclusions

We presented a computational framework to simulate the tensile and bending modes of fracture in slender beams

Table 5 Physical properties and numerical parameters used in the bent and released spaghetti problem

Property/parameter	Value
Length (L)	0.24 m
Radius (R)	0.57 mm
Mass density (ρ)	1400 kg m^{-3}
Young's modulus (E)	5.5 GPa
Critical cohesive strength (σ_c)	25 MPa
Fracture energy (G_c)	1500 N m^{-1}
Mode-mixity parameter (α)	1
Initial curvature (κ_0)	14.18 rad s^{-1}
Simulation time (T)	0.01 s
Mesh size (h)	2.4 mm
Time step (Δt)	0.1 μs
Penalty parameters ($\beta_{p,n}$ and $\beta_{t,n}$)	10

subjected to large deformations. We adopted the geometrically exact Kirchhoff beam finite element formulation by Meier et al. [37] to model the complex geometric nonlinearities involved in the beam deformation. We developed a discontinuous Galerkin discretization of the beam governing equations incorporating jumps in position and tangent degrees of freedom. In our framework, compatibility of nodal positions and tangents is weakly enforced before fracture initiation via the exchange of variationally-consistent forces and moments at the interfaces between adjacent elements. At the onset of fracture, these forces and moments transition to cohesive laws modeling softening of the stress-resultant forces and moments with the increasing interface separation. We showed that incorporating discontinuities in the tangent degrees of freedom across adjacent elements is essential for capturing beam fracture under bending. We conducted a series of numerical tests to verify our framework's ability to capture tensile and bending fracture modes in slender
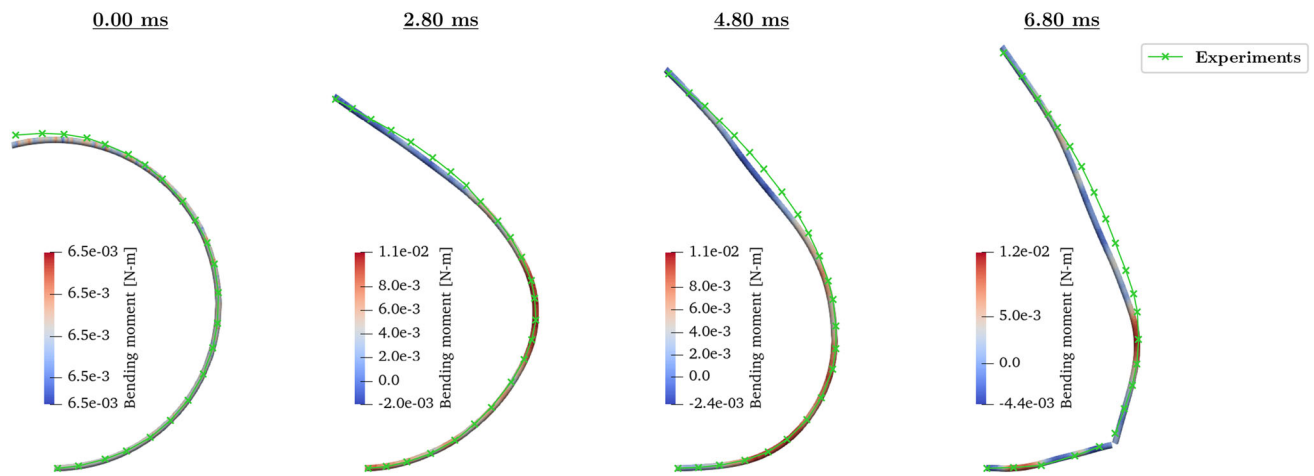
Fig. 14 Validation of our computational framework against fracture experiments of bent and released spaghetti rods [18]. The pictures show the deformed spaghetti shapes obtained in our computational predictions overlaid to those observed experimentally (green line). Our DG/CZM framework captures the local curvature build-up due to the flexural waves generated by the release, the resulting increase of bending moment (shown in the contours), as well as the ultimate fracture event. An animation of the time evolution of this simulation is provided in the Supplementary Material

beams. Finally, we applied our computational framework to reproduce experiments by Audoly and Neukirch [18] on the dynamic fracture behavior of dry spaghetti rods exhibiting large deformations.

7.1 Declaration of generative AI and AI-assisted technologies in the writing process

During the preparation of this work the author(s) used Chat-GPT in order to expedite the language editing process (e.g. to rewrite particularly complex sentences in a clearer way). After using this tool/service, the author(s) reviewed and edited the content as needed and take(s) full responsibility for the content of the publication.

A Inertia, internal, and external forces in the semi-discrete system of equations

This Appendix reports the expressions of the inertia, internal (bulk), internal (interface), and external forces discussed in Sect. 4.3.

$$M_{ab}\ddot{x}_b = \left[\int_{-1}^{1} N_a \rho A N_b \frac{L}{2}\, d\xi\right]\ddot{x}_b,$$

$$f_a^{int} = \int_{-1}^{1}\left[N_a'(EA t_1 + EI t_2) + N_a'' EI t_3\right]\frac{L}{2}\, d\xi,$$

$$f_{a\pm}^{jump} = \pm\sum_{n=1}^{E-1} \alpha_n \left[\left[N_a f_{DG,\,\|}\right] + \left[N_a'[\langle m_\perp\rangle \times t_4]\right]\right]$$

$$+\beta_p\left\langle\frac{EA}{h}\right\rangle\left[N_a c_{DG,\,\|}\right] + \beta_t\left\langle\frac{EI}{h}\right\rangle\left[N_a' t_5\right]\Big]\Big|_{S_n}$$

$$\pm\sum_{n=1}^{E-1} \gamma_n \left[\left[N_a f_{DG,\,\perp}\right]\right.$$

$$+\beta_p\left\langle\frac{EA}{h}\right\rangle\left[N_a c_{DG,\,\perp}\right]\Big]\Big|_{S_n}$$

$$\pm\sum_{n=1}^{E-1}(1-\alpha_n)\left[\left[N_a f_{coh,\,\|}\right]\right.$$

$$+\left[N_a' G_1 m_{coh,\,\perp}\right]\Big]\Big|_{S_n},$$

$$f_a^{ext} = \int_{-1}^{1}\left[N_a \tilde{f} + N_a'(\tilde{m}_\perp \times t_4)\right]\frac{L}{2}\, d\xi$$

$$+\left[N_a \bar{f}\right]\big|_{\partial_{N_f}\Omega_h} + \left[N_a'(\bar{m}_\perp \times t_4)\right]\big|_{\partial_{N_m}\Omega_h},$$

where

$$t_1 = \frac{r'}{\|r'\|}\left(\|r'\|-1\right),$$

$$t_2 = \frac{2r'(r'\cdot r'')^2}{\|r'\|^6} - \left[\frac{r'(r''\cdot r'') + r''(r'\cdot r'')}{\|r'\|^4}\right],$$

$$t_3 = \frac{r''}{\|r'\|^2} - \frac{r'(r'\cdot r'')}{\|r'\|^4},$$

$$t_4 = \frac{r'}{\|r'\|^2},$$

$$G_1 = \frac{I}{\|r'\|} - \frac{(r'\otimes r')}{\|r'\|^3},$$

$$t_5 = G_1[\![g_1]\!].$$

B Linearizations of internal and external forces

This Appendix reports the expressions of the linearization of the inertia, internal (bulk), internal (interface), and external forces discussed in Sect. 4.3.

$$K_{ab}^{int} = \frac{\partial f_a^{int}}{\partial x_b} = \int_{-1}^{1} \left[N_a' \left(EA \frac{\partial t_1}{\partial x_b} + EI \frac{\partial t_2}{\partial x_b} \right) \right.$$
$$\left. + N_a'' EI \frac{\partial t_3}{\partial x_b} \right] \frac{L}{2} \, d\xi,$$

$$K_{ab\pm}^{jump,DG} = \frac{\partial f_{a\pm}^{jump,DG}}{\partial x_b}$$
$$= \pm \sum_{n=1}^{E-1} \left[N_a EA \frac{\partial \langle t_1 \rangle}{\partial x_b} \right] \Big|_{s_n}$$
$$\pm \sum_{n=1}^{E-1} \left[N_a EI \frac{\partial \langle t_6 \rangle}{\partial x_b} \right] \Big|_{s_n}$$
$$\pm \sum_{n=1}^{E-1} \left[-N_a \left(S(\tilde{m}_\perp) \frac{\partial \langle t_4 \rangle}{\partial x_b} \right) \right] \Big|_{s_n}$$
$$\pm \sum_{n=1}^{E-1} \left[N_a' \left(S(\langle m_\perp \rangle) \frac{\partial t_4}{\partial x_b} \right) \right] \Big|_{s_n}$$
$$\pm \sum_{n=1}^{E-1} \left[-N_a' \left(S(t_4) \frac{\partial \langle m_\perp \rangle}{\partial x_b} \right) \right] \Big|_{s_n}$$
$$\pm \sum_{n=1}^{E-1} \beta_p \left\langle \frac{EA}{h} \right\rangle I \left[N_a N_b \right] \Big|_{s_n}$$
$$\pm \sum_{n=1}^{E-1} \beta_t \left\langle \frac{EI}{h} \right\rangle \left[N_a' \frac{\partial t_5}{\partial x_b} \right] \Big|_{s_n},$$

$$K_{ab}^{ext} = \frac{\partial f_a^{ext}}{\partial x_b} = \int_{-1}^{1} \left[N_a' \left(S(\tilde{m}_\perp) \frac{\partial t_4}{\partial x_b} \right) \right] \frac{L}{2} \, d\xi$$
$$+ \left[N_a' \left(S(\bar{m}_\perp) \frac{\partial t_4}{\partial x_b} \right) \right] \Big|_{\partial_{N_m} \Omega_h},$$

where $S(\cdot)$ is a skew-symmetric matrix such that $S(a)b = a \times b$ and

$$\frac{\partial t_1}{\partial x_b} = \left[\frac{(\|r'\| - 1)}{\|r'\|} I + \frac{(r' \otimes r')}{\|r'\|^3} \right] N_b',$$

$$\frac{\partial t_2}{\partial x_b} = \left[\left[\frac{2(r' \cdot r'')^2}{\|r'\|^6} - \frac{(r'' \cdot r'')}{\|r'\|^4} \right] I \right.$$
$$\left. + \left[\frac{-12(r' \cdot r'')^2}{\|r'\|^8} + \frac{4(r'' \cdot r'')}{\|r'\|^6} \right] (r' \otimes r') \right.$$
$$+ \frac{4(r' \cdot r'')}{\|r'\|^6} (r' \otimes r'') + \frac{4(r' \cdot r'')}{\|r'\|^6} (r'' \otimes r') - \frac{(r'' \otimes r'')}{\|r'\|^4} \right] N_b'$$

$$+ \left[\frac{-(r' \cdot r'')}{\|r'\|^4} I + \frac{4(r' \cdot r'')}{\|r'\|^6} (r' \otimes r') \right.$$
$$\left. - \frac{2(r' \otimes r'')}{\|r'\|^4} - \frac{(r'' \otimes r')}{\|r'\|^4} \right] N_b'',$$

$$\frac{\partial t_3}{\partial x_b} = \left[\frac{-(r' \cdot r'')}{\|r'\|^4} I + \frac{4(r' \cdot r'')}{\|r'\|^6} (r' \otimes r') - \right.$$
$$\frac{2(r'' \otimes r')}{\|r'\|^4} - \frac{(r' \otimes r'')}{\|r'\|^4} \right] N_b'$$
$$+ \left[\frac{I}{\|r'\|^2} - \frac{(r' \otimes r')}{\|r'\|^4} \right] N_b'',$$

$$\frac{\partial t_4}{\partial x_b} = \left[\frac{I}{\|r'\|^2} - \frac{2(r' \otimes r')}{\|r'\|^4} \right] N_b',$$

$$\frac{\partial m_\perp}{\partial x_b} = EI \left[-S(r'') \frac{\partial t_4}{\partial x_b} + S(t_4) N_b'' \right],$$

$$\frac{\partial t_5}{\partial x_b} = \left[G_1 G_1 - \frac{([\![g_1]\!] \otimes r')}{\|r'\|^3} - \frac{(r' \otimes [\![g_1]\!])}{\|r'\|^3} \right.$$
$$\left. - \frac{([\![g_1]\!] \cdot r')}{\|r'\|^3} I + \frac{3([\![g_1]\!] \cdot r')(r' \otimes r')}{\|r'\|^5} \right] N_b',$$

$$t_6 = t_4 \times \kappa' = \frac{2r''(r' \cdot r'')}{\|r'\|^4} + \frac{r'(r' \cdot r''')}{\|r'\|^4}$$
$$- \left[\frac{2r'(r' \cdot r'')^2}{\|r'\|^6} + \frac{r'''}{\|r'\|^2} \right],$$

$$\frac{\partial t_6}{\partial x_b} = \left[\left[\frac{-2(r' \cdot r'')^2}{\|r'\|^6} + \frac{(r' \cdot r''')}{\|r'\|^4} \right] I \right.$$
$$+ \left[\frac{12(r' \cdot r'')^2}{\|r'\|^8} - \frac{4(r' \cdot r''')}{\|r'\|^6} \right] (r' \otimes r')$$
$$- \frac{4(r' \cdot r'')}{\|r'\|^6} (r' \otimes r'') - \frac{8(r' \cdot r'')}{\|r'\|^6} (r'' \otimes r')$$
$$\left. + \frac{2(r'' \otimes r'')}{\|r'\|^4} + \frac{(r' \otimes r''')}{\|r'\|^4} + \frac{2(r''' \otimes r')}{\|r'\|^4} \right] N_b'$$
$$+ \left[\frac{2(r' \cdot r'')}{\|r'\|^4} I - \frac{4(r' \cdot r'')}{\|r'\|^6} (r' \otimes r') + \frac{2(r'' \otimes r')}{\|r'\|^4} \right] N_b''$$
$$+ \left[\frac{-I}{\|r'\|^2} + \frac{(r' \otimes r')}{\|r'\|^4} \right] N_b'''.$$

References

1. Sharma H, Kumar A, Rana S, Sahoo NG, Jamil M, Kumar R, Sharma S, Li C, Kumar A, Eldin SM et al (2023) Critical review on advancements on the fiber-reinforced composites: role of fiber/matrix modification on the performance of the fibrous composites. J Mater Res Technol 26:2975–3002

2. Grishanov S (2011) Structure and properties of textile materials. In: Clark M (ed) Handbook of textile and industrial dyeing. Elsevier, pp 28–63

3. Simon J-W (2021) A review of recent trends and challenges in computational modeling of paper and paperboard at different scales. Arch Comput Methods Eng 28(4):2409–2428

4. Deshpande V, Ashby M, Fleck N (2001) Foam topology: bending versus stretching dominated architectures. Acta Mater 49(6):1035–1040

5. Evans AG, Hutchinson JW, Fleck NA, Ashby M, Wadley H (2001) The topological design of multifunctional cellular metals. Prog Mater Sci 46(3–4):309–327

6. Bastek J-H, Kumar S, Telgen B, Glaesener RN, Kochmann DM (2022) Inverting the structure-property map of truss metamaterials by deep learning. Proc Natl Acad Sci 119(1):e2111505119

7. Li F-M, Lyu X-X (2014) Active vibration control of lattice sandwich beams using the piezoelectric actuator/sensor pairs. Compos Part B Eng 67:571–578

8. Guo Z-K, Yang X-D, Zhang W (2020) Dynamic analysis, active and passive vibration control of double-layer hourglass lattice truss structures. J Sandw Struct Mater 22(5):1329–1356

9. Meza LR, Zelhofer AJ, Clarke N, Mateos AJ, Kochmann DM, Greer JR (2015) Resilient 3D hierarchical architected metamaterials. Proc Natl Acad Sci 112(37):11502–11507

10. Abueidda DW, Al-Rub RKA, Dalaq AS, Lee D-W, Khan KA, Jasiuk I (2016) Effective conductivities and elastic moduli of novel foams with triply periodic minimal surfaces. Mech Mater 95:102–115

11. Tancogne-Dejean T, Diamantopoulou M, Gorji MB, Bonatti C, Mohr D (2018) 3D plate-lattices: an emerging class of low-density metamaterial exhibiting optimal isotropic stiffness. Adv Mater 30(45):1803334

12. Guell Izard A, Bauer J, Crook C, Turlo V, Valdevit L (2019) Ultra-high energy absorption multifunctional spinodal nanoarchitectures. Small 15(45):1903834

13. Portela CM, Edwards BW, Veysset D, Sun Y, Nelson KA, Kochmann DM, Greer JR (2021) Supersonic impact resilience of nanoarchitected carbon. Nat Mater 20(11):1491–1497

14. Kochmann DM, Bertoldi K (2017) Exploiting microstructural instabilities in solids and structures: from metamaterials to structural transitions. Appl Mech Rev 69(5):050801

15. Vangelatos Z, Gu GX, Grigoropoulos CP (2019) Architected metamaterials with tailored 3D buckling mechanisms at the microscale. Extreme Mech Lett 33:100580

16. Lu C, Hsieh M, Huang Z, Zhang C, Lin Y, Shen Q, Chen F, Zhang L (2022) Architectural design and additive manufacturing of mechanical metamaterials: a review. Engineering 17:44–63

17. Christopher S (1996) No ordinary genius: the illustrated Richard Feynman. Norton and Company Ltd., New York

18. Audoly B, Neukirch S (2005) Fragmentation of rods by cascading cracks: why spaghetti does not break in half. Phys Rev Lett 95(9):095505

19. Armero F, Ehrlich D (2006) Numerical modeling of softening hinges in thin Euler–Bernoulli beams. Comput Struct 84(10–11):641–656

20. Becker G, Noels L (2011) A fracture framework for Euler-Bernoulli beams based on a full discontinuous Galerkin formulation/extrinsic cohesive law combination. Int J Numer Methods Eng 85(10):1227–1251

21. Lai W, Gao J, Li Y, Arroyo M, Shen Y (2020) Phase field modeling of brittle fracture in an Euler-Bernoulli beam accounting for transverse part-through cracks. Comput Methods Appl Mech Eng 361:112787

22. Öchsner A (2021) Classical beam theories of structural mechanics, vol 42. Springer

23. Simo JC, Oliver J, Armero F (1993) An analysis of strong discontinuities induced by strain-softening in rate-independent inelastic solids. Comput Mech 12(5):277–296

24. Radovitzky R, Seagraves A, Tupek M, Noels L (2011) A scalable 3D fracture and fragmentation algorithm based on a hybrid, discontinuous Galerkin, cohesive element method. Comput Methods Appl Mech Eng 200(1–4):326–344

25. Francfort GA, Marigo J-J (1998) Revisiting brittle fracture as an energy minimization problem. J Mech Phys Solids 46:1319–1342

26. Bourdin B, Francfort GA, Marigo J-J (2000) Numerical experiments in revisited brittle fracture. J Mech Phys Solids 48(4):797–826

27. Ehrlich D, Armero F (2005) Finite element methods for the analysis of softening plastic hinges in beams and frames. Comput Mech 35(4):237–264

28. Bitar I, Kotronis P, Benkemoun N, Grange S (2018) A generalized Timoshenko beam with embedded rotation discontinuity. Finite Elem Anal Des 150:34–50

29. Tojaga V, Kulachenko A, Östlund S, Gasser TC (2021) Modeling multi-fracturing fibers in fiber networks using elastoplastic Timoshenko beam finite elements with embedded strong discontinuities–Formulation and staggered algorithm. Comput Methods Appl Mech Eng 384:113964

30. Meier C, Popp A, Wall WA (2019) Geometrically exact finite element formulations for slender beams: Kirchhoff–Love theory versus Simo–Reissner theory. Arch Comput Methods Eng 26(1):163–243

31. Heisser RH, Patil VP, Stoop N, Villermaux E, Dunkel J (2018) Controlling fracture cascades through twisting and quenching. Proc Natl Acad Sci 115(35):8665–8670

32. Tojaga V, Gasser TC, Kulachenko A, Östlund S, Ibrahimbegovic A (2023) Geometrically exact beam theory with embedded strong discontinuities for the modeling of failure in structures. Part I: formulation and finite element implementation. Comput Methods Appl Mech Eng 410:116013

33. Simo JC (1985) A finite strain beam formulation. The three-dimensional dynamic problem. Part I. Comput Methods Appl Mech Eng 49(1):55–70

34. Miller O, Freund L, Needleman A (1999) Modeling and simulation of dynamic fragmentation in brittle materials. Int J Fract 96:101–125

35. Zhou F, Molinari J-F, Ramesh K (2006) Effects of material properties on the fragmentation of brittle materials. Int J Fract 139(2):169–196

36. Meier C, Popp A, Wall WA (2014) An objective 3D large deformation finite element formulation for geometrically exact curved Kirchhoff rods. Comput Methods Appl Mech Eng 278:445–478

37. Meier C, Popp A, Wall WA (2015) A locking-free finite element formulation and reduced models for geometrically exact Kirchhoff rods. Comput Methods Appl Mech Eng 290:314–341

38. Meier C (2016) Geometrically exact finite element formulations for slender beams and their contact interaction. PhD thesis. Technische Universitat Munchen

39. Boyer F, Primault D (2004) Finite element of slender beams in finite transformations: a geometrically exact approach. Int J Numer Methods Eng 59(5):669–702

40. Meier C, Popp A, Wall WA (2016) A finite element approach for the line-to-line contact interaction of thin beams with arbitrary orientation. Comput Methods Appl Mech Eng 308:377–413

41. Ferri G, Ignesti D, Marino E (2023) An efficient displacement-based isogeometric formulation for geometrically exact viscoelastic beams. Comput Methods Appl Mech Eng 417:116413

42. Weeger O, Schillinger D, Müller R (2022) Mixed isogeometric collocation for geometrically exact 3D beams with elasto-visco-plastic material behavior and softening effects. Comput Methods Appl Mech Eng 399:115456

43. Camacho GT, Ortiz M (1996) Computational modelling of impact damage in brittle materials. Int J Solids Struct 33(20–22):2899–2938

44. Talamini BL, Radovitzky R (2017) A parallel discontinuous Galerkin/cohesive-zone computational framework for the simulation of fracture in shear-flexible shells. Comput Methods Appl Mech Eng 317:480–506

45. Zavattieri PD (2006) Modeling of crack propagation in thin-walled structures using a cohesive model for shell elements. J Appl Mech 73(6):948–958

46. Ortiz M, Pandolfi A (1999) Finite-deformation irreversible cohesive elements for three-dimensional crack-propagation analysis. Int J Numer Methods Eng 44:1267–1282

47. Noels L, Radovitzky R (2006) A general discontinuous Galerkin method for finite hyperelasticity. Formulation and numerical applications. Int J Numer Methods Eng 68(1):64–97

48. Hughes TJ (2012) The finite element method: linear static and dynamic finite element analysis. Courier Corporation

49. Simo JC, Vu-Quoc L (1986) A three-dimensional finite-strain rod model. Part II: computational aspects. Comput Methods Appl Mech Eng 58(1):79–116

50. Brezzi F, Manzini G, Marini D, Pietra P, Russo A (2000) Discontinuous Galerkin approximations for elliptic problems. Numer Methods Partial Differ Equ Int J 16(4):365–378

51. Noels L, Radovitzky R (2008) An explicit discontinuous Galerkin method for non-linear solid dynamics: formulation, parallel implementation and scalability properties. Int J Numer Methods Eng 74(9):1393–1420